1   **Revision 2**

2   **Behaviour and origin of hydrogen defects in natural orthopyroxene during**
3   **high-temperature processes**

4   YAN YANG[a],*, JANNICK INGRIN[a,b], WENDI LIU[a], WEIHUA HUANG[a],
5   XIAOYAN GU[a], QUNKE XIA[a]

6   [a] Key Laboratory of Geoscience Big Data and Deep Resource of Zhejiang Province, School of
7   Earth Sciences, Zhejiang University, Hangzhou 310027, China
8   [b] Univ.Lille, CNRS, INRAE, ENSCL, UMR 8207, UMET, Unité Matériaux et Transformations, F
9   59000 Lille, France
10   *Corresponding author: Yan Yang (yanyang2005@zju.edu.cn)

11   **ABSTRACT**

12   Spectral features of hydrogen defects in natural mantle minerals derive from

13   physico-chemical conditions of the lithosphere. Although hydrogen defects in

14   synthetic orthopyroxene have been well investigated, their complex spectral features

15   in natural orthopyroxenes are still difficult to decipher. To clarify this issue, it is

16   indispensable to reveal what happens to hydrogen defects during high temperature

17   processes, thereby fingerprinting the origins of hydrogen defects observed in natural

18   orthopyroxene. Here, we carry out Fourier transform infrared spectroscopic studies on

19   hydrogen defects of three natural orthopyroxenes at elevated temperatures to 1000 ^{o}C.

20   Hydrogen defects display reversible disordering at temperatures above 700 ^{o}C, which

21   is different to those at ambient conditions. Moreover, hydrogen diffusivities are

22   significantly different between the orthopyroxene samples from different tectonic

23   settings despite their similar iron contents. Even for the same crystal, different

24   hydrogen defects display different diffusion behaviors. Hydrogen defects

25   corresponding to the 3420 cm^{-1} band have the fastest diffusivity relative to the other

26   hydrogen defects. Most importantly, hydrogen defects can re-distribute in the crystal,

27   with new hydrogen defects produced at the cost of the initial hydrogen defects rather

28   than involving reaction with an external hydrogen source. Combining these findings

29   with previously reported hydrogen defects in natural olivine and clinopyroxene at

30   high temperatures, we propose that (1) to correctly relate hydrogen defects features to

31   geological processes, it is imperative to understand their behavior and origin, (2)

32   hydrogen disordering should be taken into account when predicting and extrapolating

33   data on physical properties of the mantle from room-temperature measurements.

34

INTRODUCTION

38   Nominally anhydrous minerals (NAMs) constitute a significant water reservoir

39   in the mantle (Bell and Rossman 1992; Pearson et al. 2014). Water is mainly

40   incorporated as hydrogen defects bonding to oxygen in the minerals, where hydrogen

41   acts as charge compensation for cation vacancies or heterovalent substitutions. Even

42   trace amounts of water in NAMs can strongly influence their physical properties, such

43   as electrical conductivity, thermal conductivity, elastic properties and rheology (e.g.,

44   Mackwell et al. 1985; Karato 1990; Thomas et al. 2012; Faul et al. 2016; Chang et al.

45   2017), thereby responsible for physical and chemical processes in the deep Earth

46   (Peslier et al. 2010; Xia et al. 2013; Liu et al. 2017). Orthopyroxene is the second

47   abundant constituent mineral of the upper mantle. Aluminous orthopyroxene could be

48   a more important host for water than olivine in the upper mantle, because about 8000

49   ppm by weight H_2O could be incorporated in aluminous orthopyroxene synthesized at

50   low pressures of 15 kb (Mierdel et al. 2007). Natural orthopyroxene can accommodate

51   water up to 460 ppm by weight H_2O (Demouchy and Bolfan-Casanova 2016). Several

52   studies have explored hydrogen incorporation mechanism in synthetic orthopyroxene

53   using Fourier Transform Infrared Spectroscopy (FTIR) to identify characteristic OH

54   vibration bands. For example, there are mainly two OH bands at 3360 and 3070 cm^{-1}

55   for the synthetic pure enstatite system, and additional OH bands above 3400 cm^{-1} will

56   occur for the orthopyroxene doped with cations such as Al and Cr (Prechtel and

57   Stalder 2010, 2011; Stalder et al. 2012). Cations such as Al^{3+}, Cr^{3+} and Fe^{3+} are

58   identified as potential key parameters affecting hydrogen incorporation mechanism in

59   orthopyroxene (Stalder and Skogby 2002; Stalder 2004; Stalder et al. 2005). In

60   contrast, orthopyroxene samples from the mantle usually show more complex

61   hydrogen features than synthetic orthopyroxene. Spectral features of hydrogen defects

62   in synthetic orthopyroxene samples rarely match those in natural orthopyroxene

2

63 samples, and the discrepancies between them are still not satisfactorily explained

64 (Stalder et al. 2015).

65   Because of the complexity of hydrogen defects in natural orthopyroxene, the

66 features of hydrogen defects can be used to decipher physical conditions of the

67 geological processes. Spectral features of hydrogen defects have been found to be

68 different for mantle orthopyroxenes from different geological settings. For instance,

69 the FTIR spectral signatures of hydrogen defects of orthopyroxene in spinel

70 lherzolites are different from those in garnet lherzolites, and the difference was

71 interpreted from the perspective of different oxygen fugacity by Grant et al. (2007).

72 Pyroxenes in mantle xenoliths from the Nógrád-Gömör volcanic field have anomalous

73 types of FTIR spectra, and were interpreted as relating to the young extensional

74 tectonic setting (Patkó et al. 2019). Furthermore, a variety of profiles of hydrogen

75 defects has been observed for natural orthopyroxene from core to rim. For example,

76 the diffusive loss profiles of hydrogen defects were found in the orthopyroxene from

77 mantle lherzolites and harzburgite xenoliths, which was applied to constrain the

78 annealing history of the mantle-derived xenoliths in the hosting magma (Tian et al.

79 2017). Very recently, the redox-sensitive and redox-insensitive hydrogen defects in

80 orthopyroxene from mantle harzburgite xenoliths were identified by Tollan and

81 Hermann (2019). The two groups of hydrogen defects exhibit different profiles from

82 core to rim. The redox-insensitive hydrogen defects bands at 3600 and 3395 cm^{-1}

83 show diffusive profiles with pronounced H loss at the rim. In contrast, the

84 redox-sensitive hydrogen defects bands at 3544, 3520 and 3060 cm^{-1} show increase

85 from core towards the rim. The unique behavior of the redox-sensitive hydrogen

86 defects was suggested by the authors to preserve the information of melts from

87 reduced to oxidized conditions and thus linked to oxidized arc magmas. In addition,

88 interesting evolutions from core to rim of hydrogen defects in orthopyroxene from a

89 garnet lherzolite have also been presented by Xu et al. (2019). It shows that the

90 intensity ratio of the 3546 cm^{-1} band to 3520 cm^{-1} band increases from core to rim.

91 These intricate features of hydrogen defects observed in natural orthopyroxene from

92   the mantle may indicate that hydrogen defects have experienced significant

93   modifications during magma ascent.

94   Several studies have reported site-specific diffusivities and re-distribution of

95   hydrogen defects in natural clinopyroxene and olivine at high temperatures (Ferriss et

96   al. 2016, 2018; Jollands et al. 2019; Thoraval et al. 2019; Yang et al. 2019a, 2019b).

97   In addition to distinct diffusivities of some hydrogen defects, these studies found that

98   some new hydrogen defects occurred during high temperature dehydration

99   experiments, providing new insights into features of hydrogen defects in

100   clinopyroxene and olivine from the upper mantle. Therefore, it is indispensable to

101   clarify the origin of hydrogen defects in the upper mantle minerals, which leads to

102   correlate their features with geological processes. However, there has been no such

103   studies for hydrogen defects in natural orthopyroxene. Based on the complex spectral

104   features of hydrogen defects in natural orthopyroxene and their potential links to

105   geological processes, it is important to investigate what happens to hydrogen defects

106   during high temperature processes. So far, only one study has reported high

107   temperature behavior of hydrogen defects in natural orthopyroxene (Yang et al. 2012),

108   but the temperature is lower than 500 $^{\circ}$C. In this study, we carried out high

109   temperature FTIR spectroscopic studies on hydrogen defects of three natural

110   orthopyroxenes at elevated temperatures to 1000 $^{\circ}$C. We report hydrogen disordering

111   at high temperatures, and present the site-specific diffusivities and re-distribution of

112   hydrogen defects during high temperature processes.

113   **SAMPLES AND ANALYTICAL METHODS**

114   **Sample description**

115   Three natural orthopyroxene crystals from different localities were analyzed in

116   this study. One orthopyroxene comes from a peridotite xenolith from Jiande (JD),

117   China. The Jiande alkali basalt lies within the East Cathaysia block. The peridotite

118   xenolith has protogranular texture, $Ol_{59}Opx_{25}Cpx_{14}Sp_2$ modal mineralogy (%), and

119   963 and 965 °C equilibrium temperatures calculated using the two pyroxene and

120   Ca-in-Opx geothermometers assuming a pressure of 15kbar (Hao et al. 2014). The

121   second orthopyroxene comes from a peridotite xenolith from Zealandia, New Zealand.

122   The host xenolith lies in the Dun mountain ophiolite belt (Li et al. 2018). Finally, a

123   gem-quality enstatite, formed through metamorphic-hydrothermal processes or in

124   connection with pegmatites, comes from the Morogoro region in Tanzania (Malisa

125   and Muhongo 1990). All samples were un-oriented and double polished slices. Slices

126   with thicknesses ranging from 0.16 to 0.45 mm were used for FTIR spectra

127   measurements at various temperatures. The samples from JD used for the dehydration

128   experiments are two slices of 0.162 mm and 0.165 mm thicknesses, annealed at 800

129   and 1000 $^{\circ}$C, respectively. The samples from Tanzania are slices of 0.727 mm and

130   0.967 mm thicknesses annealed at 700 and 1000 $^{\circ}$C, respectively. The samples from

131   New Zealand are slices of 0.183 mm and 0.186 mm thicknesses annealed at 700 and

132   1000 $^{\circ}$C, respectively.

Electron probe micro analyzer (EPMA)

134   The chemical compositions of the samples were determined using a 1600

135   (Shimadzu) electron microprobe at Zhejiang University (China). The analyses were

136   performed with a 15 kV accelerating voltage, 10 nA beam current and a 5 μm beam

137   diameter. Natural minerals were used as standards, and a program based on the ZAF

138   procedure was applied for data correction. Multi-point measurements were conducted

139   from core to rim of each mineral grain. The chemical compositions of the three

140   samples are shown in Table 1.

FTIR spectroscopy at varying temperatures

142   Unpolarized and polarized FTIR spectra in the frequency range 4000-2500 cm^{-1}

143   were collected using a Nicolet iS50 FTIR spectrometer coupled with a Continuum

144   microscope at Zhejiang University (China). A KBr beam-splitter and a liquid

145   nitrogen-cooled MCT-A detector were used. A total of 128 scans were accumulated

146   for each spectrum at a 4 cm^{-1} resolution. The squared aperture size was set to 50

147   μm×50 μm. Sample spectra were collected on the same selected area for each sample.

148   For the high temperature measurements, the samples were placed on a Pt foil

149   with a hole of 1.5 mm in diameter or on a sapphire plate in an Instec HS1300 heating

150   stage with CaF_2 windows, equipped with a resistance heater and an S-type

151   thermocouple. The sample was heated in N_2. The sample temperature was determined

152   with an uncertainty of less than 1 °C. The temperature was increased from 20 to

153   1000 °C using a heating rate of 15 ˚C/min. For every temperature step, the dwell time

154   was 5 minutes. A background spectrum and a sample spectrum were collected at each

155   temperature 100 ºC step.

Dehydration experiments

157   Slices of the three samples were annealed in the heating stage at desired

158   temperatures for different durations. For the samples from JD, the durations are 0, 30,

159   90, 210, 300 mins at 800 °C, and 0, 30, 90 mins at 1000 °C. For the samples from

160   Tanzania, the durations are 0, 30, 60, 120, 300, 600 mins at 700 °C, and 0, 15, 25, 55

161   mins at 1000 °C. For the samples from New Zealand, the durations are 0, 30, 90, 210,

162   480, 750 mins at 700 °C, and 0, 15 mins at 1000 °C. To avoid sample oxidized by the

163   air, the heating stage was purged with N_2 of high purity during the annealing. Fourier

164   Transform Infrared Spectroscopy measurements were carried out on the samples after

165   quenching to room temperature.

Data analysis

167   To analyze site-specific temperature dependence of hydrogen defects in the

168   samples, FTIR spectra were deconvoluted into Gaussian components using the Peakfit

169   program (ver. 4.12, Systat Software Inc.). Width, amplitude and frequency of every

170   single band are adjustable to achieve the best peakfitting. To calculate the site-specific

171   diffusivities, areas of the OH bands after annealing for different durations were

172   obtained. Since the sizes of the crystals used for the dehydration experiments are three

173   times larger than their thicknesses, the site-specific hydrogen diffusivities are fitted

174   using the one-dimensional model of diffusion from Ingrin et al. (1995). The ratio of

175   the final to initial peak area is used to obtain the ratio of the final to initial

6

176   concentration as a function of annealing duration.

177   **RESULTS**

178   **Features of hydrogen defects at ambient conditions**

179   Polarized FTIR spectra of hydrogen defects of the three samples at ambient

180   conditions are displayed in Figure 1. Five groups of OH bands can be discerned: 3590,

181   3560, 3520-3510, 3420-3410 and 3060 cm^{-1}. The polarized spectra show that all

182   bands are pleochroic, indicating that the hydrogen defects responsible for these bands

183   are all crystallographically oriented rather than caused by a hydrogen in an unoriented

184   inclusion. These OH bands are within the range of those reported based on the

185   literature compilation of mantle orthopyroxenes (Tollan and Hermann 2019). The

186   band at 3060 cm^{-1} occurs only in the orthopyroxene from Tanzania. The three samples

187   all contain the bands around 3420-3410 cm^{-1} and 3520-3510 cm^{-1}, which are

188   ubiquitous for mantle orthopyroxenes (Tollan and Hermann 2019). Additionally, the

189   two OH bands at 3590 and 3560 cm^{-1} exist in both of the orthopyroxene samples from

190   peridotite xenoliths. According to previous studies on hydrogen defects in synthetic

191   orthopyroxene (Prechtel and Stalder 2010, 2011, 2012; Stalder et al. 2015), the

192   high-wavenumber bands (>3500 cm^{-1}) are generally assigned to hydrogen defects

193   associated with Si-vacancies (e.g., pure Si-vacancies or Al-Si substitution), and the

194   low-wavenumber bands (<3500 cm^{-1}) are due to hydrogen defects associated with

195   M-vacancies. Specifically, the band at 3060 cm^{-1} in the orthopyroxene from Tanzania

196   is similar to that in the synthetic pure enstatite, and is related to hydrogen defects in

197   Mg vacancies (Stalder 2004; Prechtel and Stalder 2010). The band around 3420-3410

198   cm^{-1} has been reported in the synthetic Al-rich orthopyroxene, and increases with the

199   redistribution of ferrous iron from M1 to M2 sites (Stalder and Skogby 2007).

200   Moreover, this redistribution of ferrous iron is favored during annealing at lower

201   temperatures of 600-700 °C (Stalder and Skogby 2007). The dominant OH band at

202   3420 cm^{-1} in the enstatite from New Zealand is therefore compatible with the fact that

203   this sample experienced hydration by subduction of the oceanic lithosphere (Li et al.

204   2018). The bands around 3520 and 3560 cm^{-1} exist in the synthetic Al-containing

7

205 orthopyroxene as well (Stalder 2004), thereby should be attributed to hydrogen

206 defects coupled with Al in Si vacancies. The band around 3590 cm^{-1} also appears in

207 the synthetic pure enstatite with intensity increasing as silica activity decreasing in the

208 system, thus was assigned to four protons in a Si vacancy (Prechtel and Stalder 2011).

209 To date, incorporation mechanism of hydrogen defects in natural orthopyroxene has

210 been scarcely explored. We here infer these possible incorporation mechanisms by

211 analogy with those proposed for synthetic doped orthopyroxene samples. Considering

212 the complex compositions of nature orthopyroxenes, other minor elements such as Ti

213 and Na may also play a role in hydrogen incorporation, which has been reported in

214 olivine (Tollan et al. 2018).

215 **Features of hydrogen defects at high temperatures**

216 Figure 2 displays the unpolarized and polarized FTIR spectra of hydrogen

217 defects of the enstatite from JD heated at various temperatures. With increasing

218 temperature, the bands broaden and approach each other, thus, only one asymmetric

219 broad band at temperatures above 700 °C is visible. This variation is reversible and

220 the resolved OH bands re-appear when the sample is quenched to room temperature.

221 Comparison between the absorbances of OH bands before and after heating suggests

222 that dehydration in the crystal has happened during the heating process, especially

223 prominent for the hydrogen defects responsible for the band around 3420 cm^{-1}. The

224 consistent variations of OH absorbances along the two perpendicular directions

225 exclude the possibility of the OH bond orientation changing with temperature.

226 Hydrogen defects in the enstatite from Tanzania exhibit peculiar behavior at

227 elevated temperatures (Fig. 3). The 3520 cm^{-1} band broadens and becomes invisible at

228 temperatures above 700 °C, accompanied by the appearance of the broad band

229 centering at 3400 cm^{-1}. It could not be caused by the OH bond orientation changing

230 with increasing temperature, because the variations along the two perpendicular

231 directions are consistent. When the OH bands at 20 °C before and after heating are

232 compared, it can be observed that several new OH bands at 3460, 3360 and 3070 cm^{-1}

233 appear while the original OH bands are no longer present. Thus, the broad band

8

234 around 3400 cm^{-1} observed at high temperatures (>700 °C) must be caused by

235 disordering of hydrogen defects responsible for these new bands.

236   Figure 4 shows the FTIR spectra of hydrogen defects of the enstatite in peridotite

237 xenolith from New Zealand at elevated temperatures. The dominant OH band is

238 around 3420 cm^{-1}, which is distinct from the spectral characteristics of the OH bands

239 of the enstatite in peridotite xenolith from JD. It broadens with increasing temperature

240 and flattens at temperatures above 900 °C. After being quenched from 1000 °C, there

241 is a residual of the band around 3520 cm^{-1}, whereas the band around 3420 cm^{-1} is

242 almost invisible in the spectrum. Therefore, hydrogen defects giving rise to the 3420

243 cm^{-1} band in this sample are lost during the heating process, which is similar to the

244 behavior of hydrogen defects related to the 3420 cm^{-1} band in the enstatite from JD.

Features of hydrogen defects in quenched samples after annealing

246   Figure 5 displays the FTIR spectra of hydrogen defects in the enstatite from JD

247 after annealing at 800 and 1000 °C for different durations, respectively. The integral

248 absorbance area decreases with annealing duration, indicating dehydration during the

249 annealing. Moreover, the intensity ratio between the OH bands varies, which is

250 particular apparent after annealing at 1000 °C. For example, the 3420 cm^{-1} band

251 greatly decreases while the 3520 cm^{-1} band shows a moderate reduction. Distinct

252 responses of the OH bands to annealing suggest site-specific thermal stabilities of the

253 hydrogen defects. No new OH bands appear for this sample. In contrast, the hydrogen

254 defects in the enstatite from Tanzania present some special variations (Fig. 6). Even

255 after the initial annealing for 30 mins at 700 °C or 10 mins at 1000 °C, the 3520 cm^{-1}

256 band drastically reduces, and the bands around 3420-3410 cm^{-1} and 3060 cm^{-1} almost

257 disappear. Meanwhile, some new bands at 3546, 3460, 3360 and 3070 cm^{-1} appear.

258 They have stronger absorption along Z' direction. Furthermore, these new bands seem

259 very stable and almost unchanged with further annealing. The distinct thermal

260 stabilities of the hydrogen defects are further demonstrated by the different responses

261 of hydrogen defects in the enstatite from New Zealand (Fig. 7). The intensity ratios

262 between the OH bands vary with annealing durations. It is evident that the 3420 cm^{-1}

9

263   band drastically reduces, whereas the bands at 3560 and 3520 cm^{-1} decrease less.

264   **DISCUSSION**

265   **O-H bonding at high temperatures**

266   Since the wavenumber of an OH band reflects the strength of O-H bonding, we

267   can have an understanding of O-H bonding of the hydrogen defects in natural

268   orthopyroxene at high temperatures. The wavenumber positions of the main OH

269   bands of the three samples at elevated temperatures are examined (Fig. 8). With

270   increasing temperature, the 3590 cm^{-1} band gradually shifts to lower wavenumbers,

271   the 3520 cm^{-1} band shows little shift, while the 3420 and 3060 cm^{-1} bands shift to

272   higher wavenumbers. It is noteworthy that the evolution of the 3420 cm^{-1} band

273   displays a turning point around 500 °C. The negative wavenumber shifts of the 3590

274   cm^{-1} band with increasing temperature indicate temperature-induced lengthening and

275   weakening of the O-H bonding. In contrast, the positive wavenumber shifts of the

276   3420 and 3060 cm^{-1} bands with increasing temperature suggest temperature-induced

277   weakening of the hydrogen bonding (O-H…O) which will induce a relative

278   strengthening of the primary O-H bonding (Nakamoto et al. 1955; Xu et al. 2013).

279   The turning point around 500 °C in the evolution of the 3420 cm^{-1} band suggests that

280   the corresponding hydrogen bonding expands with increasing temperature and

281   breakdowns then ceases to expand at temperatures above 500 °C, followed by

282   dehydration. We plot wavenumber shifts to initial wavenumbers of the OH bands in

283   the orthopyroxene samples as well as other nominally anhydrous minerals from

284   previous studies in Figure 8d. A negative relationship exists. This relationship is

285   helpful for evaluating the strength of hydrogen bonding in nominally anhydrous

286   minerals. The OH bands at wavenumbers above 3450 cm^{-1} have negative

287   wavenumber shifts with increasing temperature, suggesting weak hydrogen bonding.

288   In contrast, the OH bands at wavenumber below 3450 cm^{-1} have positive wavenumber

289   shifts with increasing temperature, indicating strong hydrogen bonding. Consequently,

290   at high temperatures, the O-H bonding of hydrogen defects in Si vacancies

291   corresponding to the 3590 cm^{-1} band softens, whereas the O-H bonding of hydrogen

10

292 defects in M vacancies corresponding to the 3420 and 3060 cm^{-1} bands stiffens

293 because of the hydrogen bonding involved. In the light of evolutions of wavenumbers

294 of these OH bands, it can be expected that hydrogen defects in orthopyroxene should

295 have similar ranges of O-H bonding strength at temperatures relevant to the upper

296 mantle, which should be characterized by the broad bands at temperatures above

297 700 °C observed for the three samples.

Site-specific hydrogen diffusivities

299 To quantitively compare thermal stabilities of the hydrogen defects, we plotted

300 absorbances of the deconvoluted bands in the enstatite from JD with annealing

301 duration at 800 and 1000 °C, as well as in the enstatite from New Zealand with

302 annealing duration at 700 °C in Figure 9. With increasing annealing duration, the

303 integral absorbance of the 3420 cm^{-1} band displays the most drastic decrease for the

304 three runs, while those of the other bands present a moderate reduction. As stated

305 before, the 3420 cm^{-1} band is assigned to hydrogen defects in M vacancies, and the

306 other bands at the 3520, 3560 and 3590 cm^{-1} correspond to hydrogen defects in Si

307 vacancies. Therefore, the hydrogen defects in M vacancies and Si vacancies may have

308 contrasting thermal stabilities. To have an approximated idea about the site-specific

309 hydrogen diffusivities, diffusion coefficients of hydrogen defects corresponding to the

310 3420, 3520, 3560 and 3590 cm^{-1} bands were obtained by fitting the data using a

311 one-dimensional model of diffusion as in Ingrin et al. (1995). The diffusion

312 coefficients of these hydrogen defects at 700 and 800 °C are on the order of 10^{-13} to

313 10^{-14} m^2/s. Diffusion coefficients of the different hydrogen defects in the synthetic

314 pure enstatite from Prechtel and Stalder (2011) are included in Figure 9d for

315 comparison. Diffusion coefficients of hydrogen defects in the synthetic pure enstatite

316 are on the order of 10^{-15} m^2/s, several orders of magnitude lower than those of our

317 natural orthopyroxenes. The difference has also been observed for the bulk hydrogen

318 diffusivities between natural and synthetic pure enstatite by Stalder and Skogby

319 (2003). This is not difficult to understand considering that the natural orthopyroxenes

320 contain iron which leads to dehydration by a redox mechanism (Stalder et al. 2007).

11

321   For the synthetic orthopyroxenes in the system $MgSiO_3$-$FeSiO_3$, it was shown that the

322   rate of the redox reaction increases with iron content until a threshold value of iron

323   content of 10-12% (Stalder et al. 2007). However, for the two natural orthopyroxene

324   samples with comparable iron content from peridotite, the hydrogen diffusion

325   coefficients in the orthopyroxene from New Zealand are generally higher than those

326   in the orthopyroxene from JD. Therefore, besides iron content, other factors can affect

327   the kinetics of dehydration in natural orthopyroxenes. The different hydrogen

328   diffusivities between the two natural orthopyroxenes may be accounted by their

329   different tectonic settings. It was suggested that the orthopyroxene from New Zealand

330   has experienced later hydration by subduction of the oceanic lithosphere (Li et al.

331   2018). Hydrogen defects incorporated later at the lower temperatures near subducting

332   slabs thus may have weaker stabilities. It is also possible that these hydrogen defects

333   are unstable defects created by late-stage melt rock reaction or during reaction with

334   the host magma shortly before eruption. Another important point of our study is that

335   diffusion coefficients vary with the type of hydrogen defects, especially for the

336   hydrogen defects in M vacancies responsible for the 3420 cm^{-1} band which has the

337   fastest diffusivity. It has also been found that Fe-related hydrogen defects and

338   Fe-unrelated hydrogen defects have different thermal stabilities (Stalder and Skogby

339   2007). The different diffusivities between hydrogen defects have been also observed

340   in FTIR spectra of natural orthopyroxene grains analyzed from core to rim (Tian et al.

341   2017). We do not know the accurate diffusivities of the different hydrogen defects in

342   Tian et al. (2017), but the site-specific hydrogen diffusion coefficients in our study

343   indicate that the differences are generally around one order of magnitude. These

344   differences are comparable to differences in the site-specific diffusivities of hydrogen

345   defects in natural clinopyroxene and olivine (Ferriss et al. 2016; Thoraval et al. 2019),

346   but are up to two orders of magnitude lower than difference in diffusivities between

347   magnesium vacancies and pure Si vacancies in the synthetic forsterite

348   (Padrón-Navarta et al. 2014). In contrast, the hydrogen defects corresponding to the

349   3067, 3362. 3592 and 3687 cm^{-1} band of the synthetic pure enstatite show almost the

350   same diffusivities (Fig. 9). It thus has been suggested that the hydrogen defects in M

12

351   vacancies and Si vacancies of synthetic orthopyroxene possibly have similar

352   diffusivities (Prechtel and Stalder 2011).

353   **Re-distribution of hydrogen defects during dehydration**

354   The most striking feature of hydrogen defects in the three orthopyroxenes is the

355   appearance of the new OH bands at 3546, 3460, 3360 and 3070 cm^{-1} with annealing

356   duration at the cost of the original OH bands at 3520, 3420 and 3060 cm^{-1} observed in

357   the enstatite from Tanzania. We exclude possible changes of O-H directions based on

358   the consistent variations of OH absorbances along the two perpendicular directions.

359   Additionally, possible phase transition does not occur within the temperature range

360   based on the high temperature Raman spectra of this sample (Fig. S1). Therefore, the

361   variations in the absorption of the OH bands reflect destruction and generation of

362   hydrogen defects through inter-site reaction. As stated before, the 3520 cm^{-1} band is

363   assigned to hydrogen coupled with Al in Si vacancies, while the 3420 and 3060 cm^{-1}

364   bands correspond to hydrogen related to M vacancies. The reduction of the

365   absorbances of these bands suggest loss of the corresponding hydrogen defects.

366   Meanwhile, the appearance of the new bands indicates gain of some new hydrogen

367   defects. These new bands are not frequently observed in mantle samples, but they

368   have been found in synthetic samples (Stalder and Skogby 2002; Rauch and Keppler

369   2002; Stalder 2004). Thus, these new OH bands can be currently assigned with

370   analogy to those synthetic orthopyroxenes. Since the 3546 cm^{-1} band appeared in

371   Al-doped orthopyroxene, it may correspond to hydrogen defects coupled with Al^{3+} in

372   Si vacancies. The 3460 cm^{-1} band occurred in Fe-doped orthopyroxene. Considering

373   that the dehydration mechanism of orthopyroxene usually involves the oxidation of

374   Fe^{2+} to Fe^{3+} (Stalder et al. 2007), the new band at 3460 cm^{-1} in this study could be a

375   new hydrogen defect in Si vacancies, coupled with the Fe^{3+} formed during

376   dehydration. Indeed, based on the observation on the synthetic orthopyroxene doped

377   with Al and Fe, the Fe^{3+}-related 3460 cm^{-1} band increases when the dehydrated

378   sample is annealed in H$_2$ (Stalder and Skogby 2007). The 3360 and 3070 cm^{-1} bands

379   are common in pure enstatite, thereby, the new 3360 and 3070 cm^{-1} bands may

13

380 correspond to hydrogen defects in M vacancies. Although still residing in Si vacancies
381 and M vacancies, these new hydrogen defects should have different local
382 environments compared to the original ones because of the complex interactions with
383 trivalent cations in natural orthopyroxene (Stalder et al. 2005). Other minor elements
384 such as Ti and Na may also be responsible for these defects. It should be noted that
385 these assignments with analogy to those synthetic orthopyroxenes may not always
386 work for natural samples. For example, most natural mantle orthopyroxenes
387 containing Al do not typically show the 3546 cm^{-1} band in their IR spectra based on
388 the literature compilation of mantle orthopyroxene from a wide range of tectonic
389 settings (Tollan and Hermann 2019). However, the 3546 cm^{-1} band has been reported
390 in some Al-bearing natural mantle orthopyroxenes (e.g., Grant et al. 2007; Tollan and
391 Hermann 2019; Xu et al. 2019). Anyway, the dehydration experiments in our study
392 evidence a re-distribution of hydrogen defects at high temperatures in natural
393 orthopyroxene samples. Hence, hydrogen does not always diffuse out of the crystal at
394 high temperatures, but may redistribute between different defects.
395 Temperature-induced re-distribution of hydrogen defects not only occurs in this
396 natural orthopyroxene, but was also reported in natural olivine and clinopyroxene. For
397 instance, Ferriss et al. (2018) observed hydrogen re-distribution between the [Fe^{3+}-H]
398 and pure Si vacancies in natural olivine after annealing 8 h at 800 °C. Coincidently,
399 the dehydration experiments of natural olivine revealed that hydrogen released from
400 titanium-clinohumite defects moved to pure Si vacancies, and Mg vacancies coupling
401 with trivalent cations (Yang et al. 2019b). The inter-site reactions of hydrogen defects
402 were further reported in natural olivine by Jolland et al. (2019). For natural
403 clinopyroxene, several studies reported that a new hydrogen defect coupled with Fe^{3+}
404 in M vacancies appeared accompanying loss of other hydrogen defects (Skogby and
405 Rossman 1989; Ferriss et al. 2016; Yang et al. 2019a). All in all, this study along with
406 previous studies on olivine and clinopyroxene suggests that hydrogen defects
407 observed in upper mantle minerals may have experienced complex variations during
408 high-temperature processes.

14

409   **IMPLICATIONS**

410   **Implications for fingerprinting hydrogen of different origins**

411   The most important findings of this study are the site-specific diffusivities and

412   re-distribution of hydrogen defects in natural orthopyroxene during high temperature

413   processes, improving our understanding of spectral features of hydrogen defects in

414   orthopyroxene from the mantle. Numerous studies have been carried out to explore

415   the correlation between water concentrations and tectonic settings (e.g., Skogby et al.

416   1990; Peslier et al. 2002; Grant et al. 2007; Sundvall and Stalder 2011; Demouchy and

417   Bolfan-Casanova 2016; Patkó et al. 2019), but the relationship is still unclear, partly

418   because hydrogen defects in the host minerals may be modified during their ascent

419   from the source region. In contrast to water concentration, characters of hydrogen

420   defects in the mantle minerals from different geological settings are scarcely noticed.

421   It is well known that different OH bands of the FTIR spectra represent different

422   modes of hydrogen defects incorporated in the minerals (e.g., Beran and Putnis 1983).

423   Many cases indicate that FTIR spectral signals of hydrogen defects in the upper

424   mantle minerals from different geological settings are not persistent. Along with

425   previous reports of site-specific diffusivities and re-distribution of hydrogen defects in

426   olivine and clinopyroxene, this study sheds light to the fingerprinting of different

427   processes generating hydrogen defects.

428   It is common that the dominant spectrum type in pyroxene from the mantle

429   peridotite is characterized by reducing intensities of OH bands from higher to lower

430   wavenumbers, hence, the 3420 cm^{-1} band usually is not the most predominant.

431   Exceptionally, the FTIR spectra orthopyroxene from New Zealand in this study are

432   dominated by the 3420 cm^{-1} band, which is little affected by the pleochroism. The

433   abnormal hydrogen features are not difficult to be understood considering the nature

434   of the 3420 cm^{-1} band and geological settings the host minerals experienced. Our

435   study finds that hydrogen defects corresponding to the 3420 cm^{-1} band have the

436   fastest diffusivities for mantle orthopyroxene. This finding may account for the

437   relatively weaker intensity of this band in most mantle orthopyroxenes which have

15

438   experienced outgassing during their transport to the surface (e.g., Tian et al. 2017; Xu

439   et al. 2019). Furthermore, previous dehydration experiment for synthetic

440   orthopyroxene shows that the 3420 cm^{-1} band intensity increases during the initial

441   annealing at lower temperatures (Stalder and Skogby 2007), indicating that hydrogen

442   can be re-introduced into the relevant M site at appropriate conditions. Thus, the

443   dominant 3420 cm^{-1} band of the orthopyroxene from New Zealand should be ascribed

444   to hydrogen incorporated later, either through sample hydration by subduction of the

445   oceanic lithosphere as suggested by Li et al. (2018), or during late-stage melt rock

446   reaction or during reaction with the host magma shortly before eruption. Thus, the

447   3420 cm^{-1} band may be a potential indicator of later hydrogen incorporation.

448   Additionally, it has been reported that hydrogen defects of Si vacancies in olivine is

449   favored by high water activity conditions (Tollan et al. 2017). Consequently, to

450   understand abnormal FTIR spectral signals of hydrogen defects in pyroxene such as

451   those presented in Patkó et al. (2019), site-specific hydrogen diffusivities, tectonic

452   settings, and site-specific hydrogen solubilities of pyroxene should be taken into

453   account together.

454   Besides site-specific hydrogen diffusivities, temperature-induced re-distribution

455   of hydrogen defects in upper mantle minerals has implications for deciphering

456   hydrogen defects of different origins. This study evidences the appearance of several

457   new OH bands at 3546, 3460, 3360 and 3070 cm^{-1} at the cost of the initial 3520, 3420

458   and 3060 cm^{-1} bands, and hydrogen defects corresponding to these new bands are

459   very stable. Therefore, if observed in natural orthopyroxenes, these hydrogen defects

460   may be at least partly inherited from the initial hydrogen defects. The 3546 cm^{-1} band

461   is not always observed for natural orthopyroxenes. Several studies have reported this

462   band in mantle orthopyroxenes and its height variation from core to rim (Grant et al.

463   2007; Tollan and Hermann 2019; Xu et al. 2019). In contrast to the 3546 cm^{-1} band,

464   the 3460 cm^{-1} band is scarcely observed in natural mantle orthopyroxenes. Our study

465   indicates that these hydrogen defects can be produced by inter-site reactions, without

466   involving reaction with water in the external environments such as fluid or melt.

467 Along with inter-site reactions of hydrogen defects in natural olivine and
468 clinopyroxene observed by previous studies (Skogby and Rossman 1989, Ferriss et al.
469 2016, 2018; Jolland et al. 2019; Yang et al. 2019a, 2019b), temperature-induced
470 re-distribution of hydrogen defects in natural orthopyroxene opens a new window for
471 deciphering these hydrogen defects if observed in natural mantle minerals.

472 **Implications for the physical properties of the mantle**

473 The spectroscopic data of this study suggest that the hydrogen defects in natural
474 orthopyroxene would have a constant O-H bonding strength at high temperatures but
475 display disordering at temperatures above 700 $^{\circ}$C. This finding is in agreement with
476 previous conclusions about hydrogen disordering in olivine and clinopyroxene at high
477 temperatures (Yang et al. 2019a, 2019b). To apply to the simultaneously high
478 temperature and high pressure conditions of the upper mantle, pressure effects should
479 be considered. Since high pressure FTIR spectra of hydrogen defects in the natural
480 orthopyroxene with trace amount of water are difficult to be measured using diamond
481 anvil cell (DAC), we cannot evaluate disordering degree at high pressure in this study.
482 But previous spectroscopic studies on hydrogen defects in olivine and ringwoodite at
483 high pressure indicate that pressure also induces hydrogen disordering (Panero et al.
484 2013; Yang et al. 2019b). Moreover, water concentration has been suggested to
485 enhance hydrogen disordering in wadsleyite as well (Kohn et al. 2002). Consequently,
486 taking the factors of temperature, pressure and water concentration in the mantle into
487 account, hydrogen defects should be disordered, which is different from their nature
488 observed at ambient conditions. Consequently, hydrogen disordering in mantle
489 minerals at high temperature and high pressure should be taken into account when
490 predicting and extrapolating data on physical properties from room-temperature
491 measurements.

492 **ACKNOWLEDGEMENTS**

17

500   **REFERENCES**

501   Bell, R. D., and Rossman, G. R. (1992) Water in Earth's mantle: The role of nominally
502   anhydrous minerals. Science, 255, 1391-1397.

503   Beran, A., and Putnis, A. (1983) A model of the OH position in olivine, derived from
504   infrared spectroscopy investigations. Physics and Chemistry of Minerals, 9,
505   57-60.

506   Chang, Y. Y., Hsieh, W. P., Tan, E., and Chen, J. H. (2017) Hydration-reduced lattice
507   thermal conductivity of olivine in Earth's upper mantle. Proceedings of the
508   National Academy of Sciences of the United States of America, 114, 4078.

509   Demouchy, S., and Bolfan-Casanova, N. (2016) Distribution and transport of
510   hydrogen in the lithospheric mantle: A review. Lithos, 240-243, 402-425.

511   Faul, U., Cline, C. J., David, E. C., Berry, A. J., and Jackson, I. (2016)
512   Titanium-hydroxyl defect-controlled rheology of the Earth's upper mantle. Earth
513   and Planetary Science Letters, 452, 227-237.

514   Ferriss, E., Plank, T., and Walker, D. (2016) Site-specific hydrogen diffusion rates
515   during clinopyroxene dehydration. Contributions to Mineralogy and Petrology,
516   171, 1-24.

517   Ferriss, E., Plank, T., Newcombe, M., Walker, D., and Hauri E. (2018) Rates of
518   dehydration of olivines from San Carlos and Kilauea Iki. Geochimica et
519   Cosmochimica Acta, 242, 165-190.

520   Grant, K., Ingrin, J., Lorand, J. P., and Dumas, P. (2007) Water partitioning between
521   mantle minerals from peridotite xenoliths. Contributions to Mineralogy and
522   Petrology, 154, 15-34.

523   Hao, Y., Xia, Q., Li, Q., Chen, H., and Feng, M. (2014) Partial melting control of
524   water contents in the Cenozoic lithospheric mantle of the Cathaysia block of
525   South China. Chemical Geology, 380, 7-19.

526   Ingrin, J., Hercule, S., and Charton, T. (1995) Diffusion of hydrogen in diopside:
527   Results of dehydration experiments. Journal of Geophysical Research, 100,
528   15489-15499.

529   Jollands, M. C.，Kempf, E., Hermann, J., and Müntener, O. (2019) Coupled inter-site
530   reaction and diffusion: Rapid dehydrogenation of silicon vacancies in natural
531   olivine. Geochimica et Cosmochimica Acta, 262, 220-242.

18

532   Karato, S. (1990) The role of hydrogen diffusivity in the electrical conductivity of the
533   upper mantle. Nature, 347, 272-273.

534   Kohn, S. C., Brooker, R. V., Frost, D. J., Slesinger, A. E., and Wood, B. G. (2002)
535   Ordering of hydroxyl defects in hydrous wadsleyite (β-Mg_2SiO_4). American
536   Mineralogist, 87, 293-301.

537   Li, P., Scott, J. M., Liu, J., and Xia, Q. (2018) Lateral H_2O variation in the Zealandia
538   lithospheric mantle controls orogen width. Earth Planetary Science Letters, 502,
539   200-209.

540   Liu, J., Xia, Q. K., Kuritani, T., Hanski, E., and Yu, H. R. (2017) Mantle hydration
541   and the role of water in the generation of large igneous provinces. Nature
542   Communications, 8, 1824.

543   Liu, W. D., Yang, Y., Zhu, K., and Xia, Q. K. (2018) Temperature dependences of
544   hydrous species in feldspars. Physics and Chemistry of Minerals, 45, 609-620.

545   Lu, R., and Keppler, H. (1997) Water solubility in pyrope in 100 kbar. Contributions
546   to Mineralogy and Petrology, 129, 35-42.

547   Mackwell, S. J., Kohlstedt, D. L., and Paterson, M. S. (1985) The role of water in the
548   deformation of olivine single crystals. Journal of Geophysical Research, 90,
549   11319-11333.

550   Malisa, E., and Muhongo, S. (1990) Tectonic Setting of Gemstone Mineralization in
551   the Proterozoic Metamorphic Terrane of the Mozambique Belt in Tanzania.
552   Precambrian Research, 46, 167-176.

553   Mierdel, K., Keppler, H., Smyth, J.R., and Langenhorst, F. (2007) Water solubility in
554   aluminous orthpyroxene and the origin of the Earth's asthenosphere. Science,
555   315, 364-368.

556   Nakamoto, K., Margosches, M., and Rundle, R. E. (1955) Stretching frequencies as a
557   function of distances in hydrogen bonds. Journal of American Chemical Society,
558   77, 6480-6486.

559   Rauch, M., and Keppler, H. (2002) Water solubility in orthopyroxene. Contributions
560   to Mineralogy and Petrology, 143, 525-536.

561   Padrón-Navarta, J. A., Hermann, J., and O'Neill, H. S. C. (2014) Site-specific
562   hydrogen diffusion rates in forsterite. Earth and Planetary Science Letters, 392,
563   100-112.

564   Panero, W. R., Smyth, J. R., Pigott, J. S., Liu, Z., and Frost, D. J. (2013). Hydrous
565   ringwoodite to 5 K and 35 GPa: Multiple hydrogen bonding sites resolved with
566   FTIR spectroscopy. American Mineralogist, 98, 637-642.

567   Patkóa, L., Liptai, N., Kovác,s I., Aradia, L. E., Xia, Q. K., Ingrin, J., Mihály, J.,
568   O'Reilly, S. Y., Griffin, W. L., Wesztergom, V., and Szabó, C. (2019) Extremely
569   low structural hydroxyl contents in upper mantle xenoliths from the

19

570   Nógrád-Gömör Volcanic Field (northern Pannonian Basin): Geodynamic
571   implications and the role of post-eruptive re-equilibration. Chemical Geology,
572   507, 23-41.

573 Pearson, D. G., Brenker, F. E., Nestola, F., Mcneill, J., Nasdala, L., Hutchison M. T.,
574   Matveev, S., Mather, K., Silversmit, G., Schmitz, S., Vekemans, B., and Vincze,
575   L. (2014) Hydrous mantle transition zone indicated by ringwoodite included
576   within diamond. Nature, 507 (7491), 221-224.

577 Peslier, A. H., Luhr, J. F., and Post, J. (2002) Low water contents in pyroxenes from
578   spinel-peridotites of the oxidized, sub-arc mantle wedge. Earth and Planetary
579   Science Letters, 201, 69-86.

580 Peslier, A. H., Woodland, A. B., Bell, D. R., and Lazarov, M. (2010) Olivine water
581   contents in the continental lithosphere and the longevity of cratons. Nature, 467,
582   78-U108.

583 Prechtel, F., and Stalder, R. (2010) FT-IR spectroscopy with focal plane array detector
584   - A novel tool to monitor the spatial OH-defect distribution in single crystals
585   applied to synthetic enstatite. American Mineralogist, 95, 888-891.

586 Prechtel, F., and Stalder, R. (2011) The potential use of OH-defects in enstatite as
587   geobarometer. Contributions to Mineralogy and Petrology, 162, 615-623.

588 Prechtel, F., and Stalder, R. (2012) OH-defects in Al- and Cr- doped synthetic
589   enstatites and defect geobarometry on natural orthopyroxenes from Earth's
590   mantle. European Journal of Mineralogy, 24, 471-481.

591 Skogby, H., and Rossman, G. R. (1989) OH⁻ in pyroxene: An experimental study of
592   incorporation mechanisms and stability. American Mineralogist, 74, 1059-1069.

593 Skogby, H., Bell, D. R., and Rossman, G. R. (1990) Hydroxide in pyroxene: variations
594   in the natural environment. American Mineralogist, 75, 767-774.

595 Stalder, R. (2004) Influence of Fe, Cr and Al on hydrogen incorporation in
596   orthopyroxene. European Journal of Mineralogy, 16, 703-711.

597 Stalder, R., and Skogby, H. (2002) Hydrogen incorporation in enstatite. European
598   Journal of Mineralogy, 14, 1139-1144.

599 Stalder, R., and Skogby, H. (2007) Dehydration mechanisms in synthetic Fe-bearing
600   enstatite. European Journal of Mineralogy, 19, 201-21.

601 Stalder, R., Klemme, S., Ludwig, T., and Skogby, H. (2005) Hydrogen incorporation
602   in orthopyroxene: interaction of different trivalent cations. Contributions to
603   Mineralogy and Petrology, 150, 473-485.

604 Stalder, R., Purwin, H., and Skogby, H. (2007) Influence of Fe on hydrogen
605   diffusivity in orthopyroxene. European Journal of Mineralogy, 19, 899-904.

606 Stalder, R., Prechtel, F., and Ludwig, T. (2012) No site-specific infrared absorption
607   coefficients for OH-defects in pure enstatite. European Journal of Mineralogy, 24,

608   465-470.

609 Stalder, R., Karimova, A., and Konzett, J. (2015) OH-defects in multiple-doped
610   orthoenstatite at 4-8 GPa: filling the gap between pure and natural systems.
611   Contributions to Mineralogy and Petrology, 169, 38.

612 Sundvall, R., and Stalder, R. (2011) Water in upper mantle pyroxene megacrysts and
613   xenocrysts: a survey study. American Mineralogist, 96, 1215-1227.

614 Thomas, S. M., Bina, C. R., Jacobsen, S. D., and Goncharov, A. F. (2012) Radiative
615   heat transfer in a hydrous mantle transition zone. Earth and Planetary Science
616   Letters, 357, 130-136.

617 Thoraval, C., Demouchy, S., and Padrón-Navarta, J. A. (2019) Relative diffusivities of
618   hydrous defects from a partially dehydrated natural olivine. Physics and
619   Chemistry of Minerals, 46, 1-13.

620 Tian, Z. Z., Liu, J., Xia, Q. K., Ingrin, J., Hao, Y. T., and Christophe, D. (2016) Water
621   concentration profiles in natural mantle orthopyroxenes: A geochronometer for
622   long annealing of xenoliths within magma. Geology, 45, 87-90

623 Tollan, P. M., Smith, R., O'Neill, H. S. C., and Hermann, J. (2017) The responses of
624   the four main substitution mechanisms of H in olivine to H_2O activity at 1050°C
625   and 3 GPa. Progress in Earth and Planetary Science, 4(1), 14.

626 Tollan, P. M., O' Neill, H. S. C., and Hermann, J. (2018) The role of trace elements in
627   controlling H incorporation in San Carlos olivine. Contributions to Mineralogy
628   and Petrology, 173, 89.

629 Tollan, P. M., and Hermann, J. (2019) Arc magmas oxidized by water dissociation and
630   hydrogen incorporation in orthopyroxene. Nature Geoscience, 12, 667-671.

631 Xia, Q. K., Liu, J., Liu, S. C., Kovács, I., Feng, M., and Dang, L. (2013) High water
632   content in Mesozoic primitive basalts of the North China Craton and
633   implications on the destruction of cratonic mantle lithosphere. Earth and
634   Planetary Science Letters, 361, 85-97.

635 Xu, H., Zhao, Y., Hickmott, D. D., Lane, N. J., Vogel, S. C., Zhang, J., and Daemen, L.
636   L. (2013) High-temperature neutron diffraction study of deuterated brucite.
637   Physics and Chemistry of Minerals, 40, 799-810.

638 Xu, Y., Wang, W., Hui, H., Rudnick, R. L., Shang, S., and Zhang, Z. (2019)
639   Reconciling the discrepancy between the dehydration rates in mantle olivine and
640   pyroxene during xenolith emplacement. Geochimica et Cosmochimica Acta, 267,
641   179-195

642 Yang, Y., Xia, Q., Feng, M., and Liu, S. (2012) OH in nature orthopyroxene: an in situ
643   FTIR investigation at varying temperatures. Physics and Chemistry of Minerals,
644   39, 413-418.

645 Yang, Y., Ingrin, J., Xia, Q. K., and Liu, W. D. (2019a) Nature of hydrogen defects in

646   clinopyroxenes from room temperature up to 1000 °C: Implication for the
647   preservation of hydrogen in the upper mantle and impact on electrical
648   conductivity. American Mineralogist, 104, 79-93.
649 Yang, Y., Liu, W. D., Qi, Z. M., Wang, Z. P., Smyth, J. R., and Xia, Q. K. (2019b)
650   Re-configuration and interaction of hydrogen sites in olivine at high temperature
651   and high pressure. American Mineralogist, 104, 878-889.

652

653

654   **Table 1 Chemical compositions of the three orthopyroxenes**

Sample	SiO_2	TiO_2	Al_2O_3	Cr_2O_3	FeO	MnO	MgO	CaO	Na_2O	K_2O	NiO	Total
JD	54.65	0.15	4.79	0.34	6.50	0.11	32.01	0.71	0.10	0.00	0.08	99.77
Tanzania	57.44	0.02	0.05	0.01	6.64	0.21	34.75	0.11	0.02	0.00	0.01	99.27
New Zealand	55.23	0.02	3.17	0.73	6.06	0.12	33.22	1.04	0.04	0.02	0.18	99.81

655

656   **Figure captions**

657   **Figure 1** (a)-(c) Polarized FTIR spectra of hydrogen defects of the three orthopyroxenes from JD,
658   Tanzania, and New Zealand at room temperature. The spectra are normalized to 1 cm thickness.
659   (a')-(c') spectra of the Si-O overtones of the orthopyroxenes with the polarizer rotated at two
660   perpendicular angles. The X', Y' and Z' indicate the directions obtained by comparing the spectra
661   of the Si-O overtones with Prechtel and Stalder (2012).

662   **Figure 2** FTIR spectra of hydrogen defects in the enstatite from JD analyzed at various
663   temperatures: (a) unpolarized spectra; (b) and (c) spectra collected with the polarizer rotated at
664   two perpendicular angles. The X' and Y' indicate the directions obtained by comparing the spectra
665   of the Si-O overtones with Prechtel and Stalder (2012). The spectra are shifted vertically for
666   clarity.

667   **Figure 3** FTIR spectra of hydrogen defects in the enstatite from Tanzania analyzed at various
668   temperatures: (a) unpolarized spectra; (b) and (c) spectra collected with the polarizer rotated at
669   two perpendicular angles. The X' and Z' indicate the directions obtained by comparing the spectra
670   of the Si-O overtones with Prechtel and Stalder (2012). The spectra are shifted vertically for clarity.
671   The arrow indicates the appearance of the new bands. The new bands at high temperatures are
672   indicated by the yellow boxes.

673   **Figure 4** FTIR spectra of hydrogen defects in the enstatite from New Zealand analyzed at various
674   temperatures: (a) unpolarized spectra; (b) and (c) spectra collected with the polarizer rotated at
675   two perpendicular angles. The X' and Z' indicate the directions obtained by comparing the spectra
676   of the Si-O overtones with Prechtel and Stalder (2012). The spectra are shifted vertically for
677   clarity.

22

678   **Figure 5** Unpolarized and polarized FTIR spectra of the enstatite from JD annealed at 800 and
679   1000 ^{o}C. The spectra are normalized to 1 cm thickness. The Y' and Z' indicate the directions
680   obtained by comparing the spectra of the Si-O overtones with Prechtel and Stalder (2012).

681   **Figure 6** Unpolarized and polarized FTIR spectra of the enstatite from Tanzania annealed at 700
682   and 1000 ^{o}C. The spectra are normalized to 1 cm thickness. The X' and Z' indicate the directions
683   obtained by comparing the spectra of the Si-O overtones with Prechtel and Stalder (2012). The
684   new bands are indicated by the colored rectangles.

685   **Figure 7** Unpolarized and polarized FTIR spectra of the enstatite from New Zealand annealed at
686   700 and 1000 ^{o}C. The 3700 cm^{-1} band should be the signal of coexisting hydrous minerals. The
687   spectra are normalized to 1 cm thickness. The X', Y' and Z' indicate the directions obtained by
688   comparing the spectra of the Si-O overtones with Prechtel and Stalder (2012).

689   **Figure 8** (a) to (c) Evolutions of OH wavenumbers with increasing temperature for the enstatite
690   from JD, Tanzania and New Zealand, respectively; (d) relationship between temperature-induced
691   wavenumber shift (dv/dT) with initial wavenumber for the common NAMs in the crust and mantle.
692   dv/dT is the change in wavenumber divided by the change in temperature. Their values are fitted
693   from the relationships between wavenumber and temperature. Clinopyroxenes data indicated by
694   red symbols are from Yang et al. (2019a). Pyrope data are from Lu and Keppler (1997). Olivine
695   data are from Yang et al. (2019b). Feldspar data are from Liu et al. (2018). The data from this
696   study are indicated by the green symbols.

697   **Figure 9** (a)-(c) Variations of integral absorbances of OH bands in enstatites from JD and New
698   Zealand with annealing duration; (d) site-specific diffusion coefficients of the hydrogen defects in
699   natural enstatite from JD at 800 ^{o}C and from New Zealand at 700 ^{o}C. The site-specific diffusion
700   coefficients of hydrogen defects at 800 ^{o}C in the synthetic pure enstatite (Prechtel and Stalder
701   2011), in the natural diopside (Ferriss et al. 2016) and synthetic forsterite (Padrón-Navarta et al.
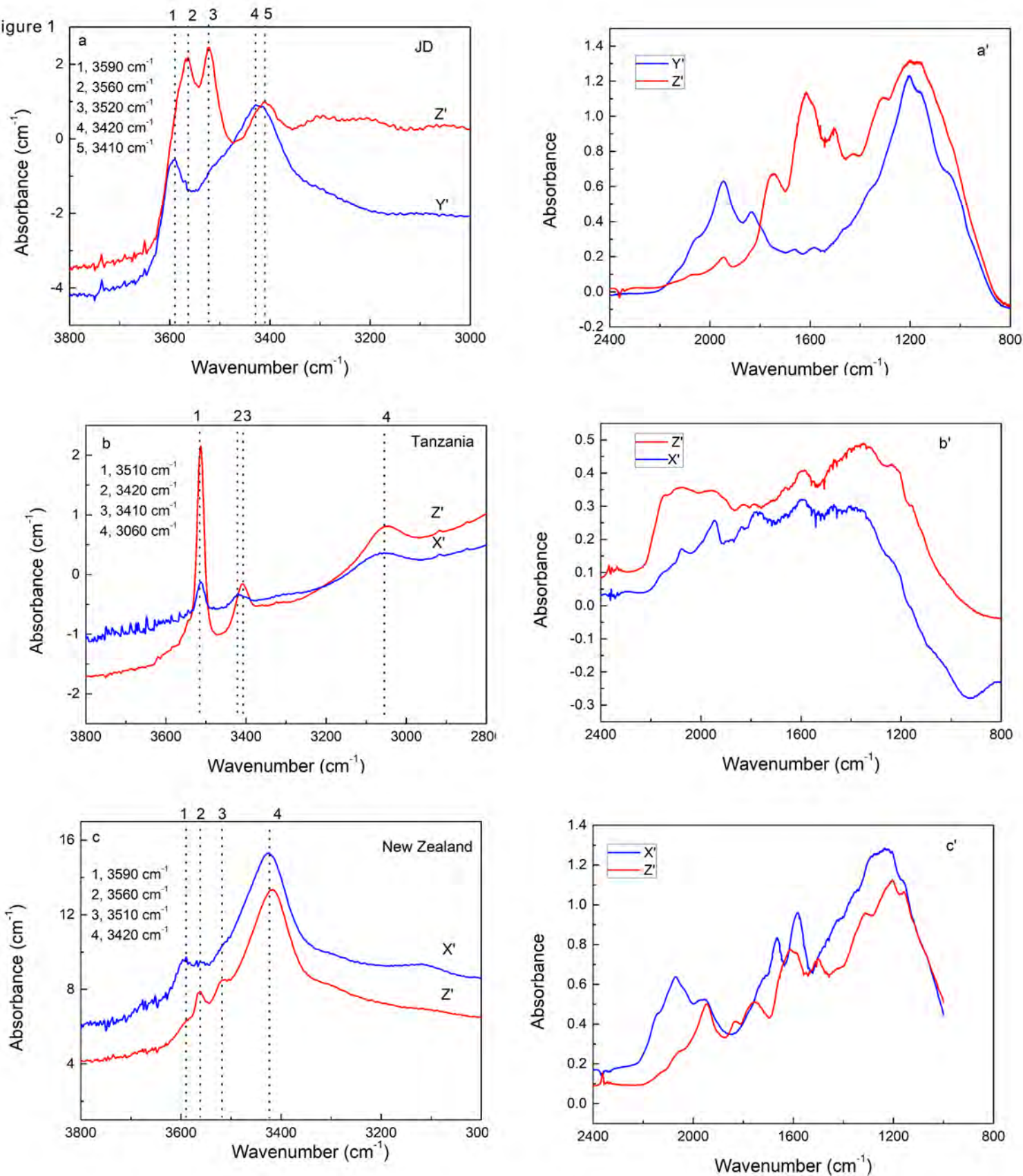702   2014) are shown for comparison.
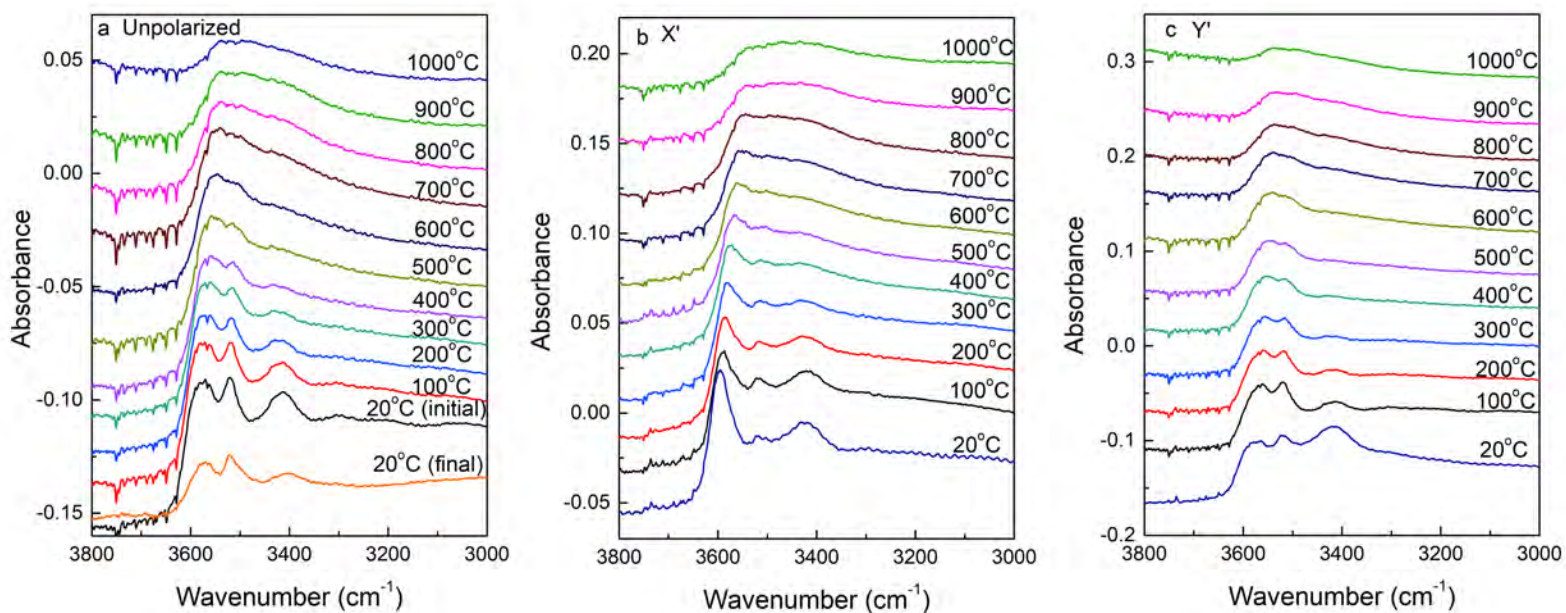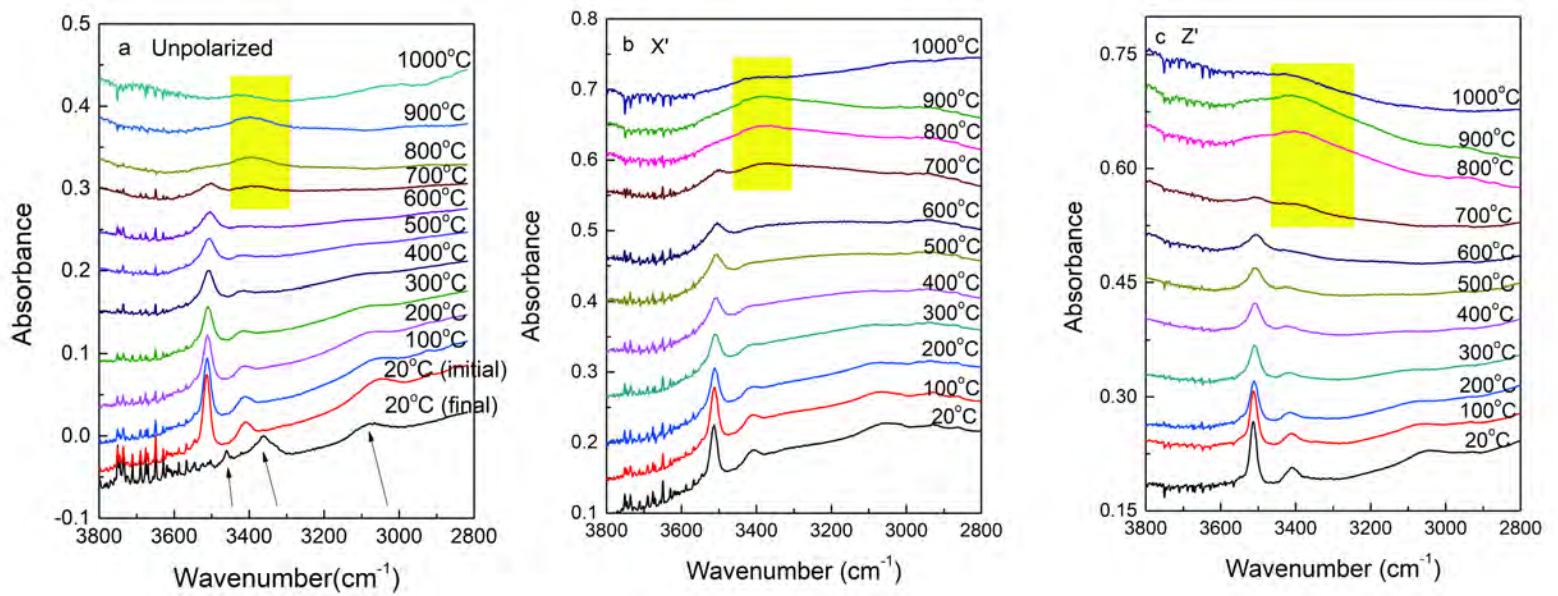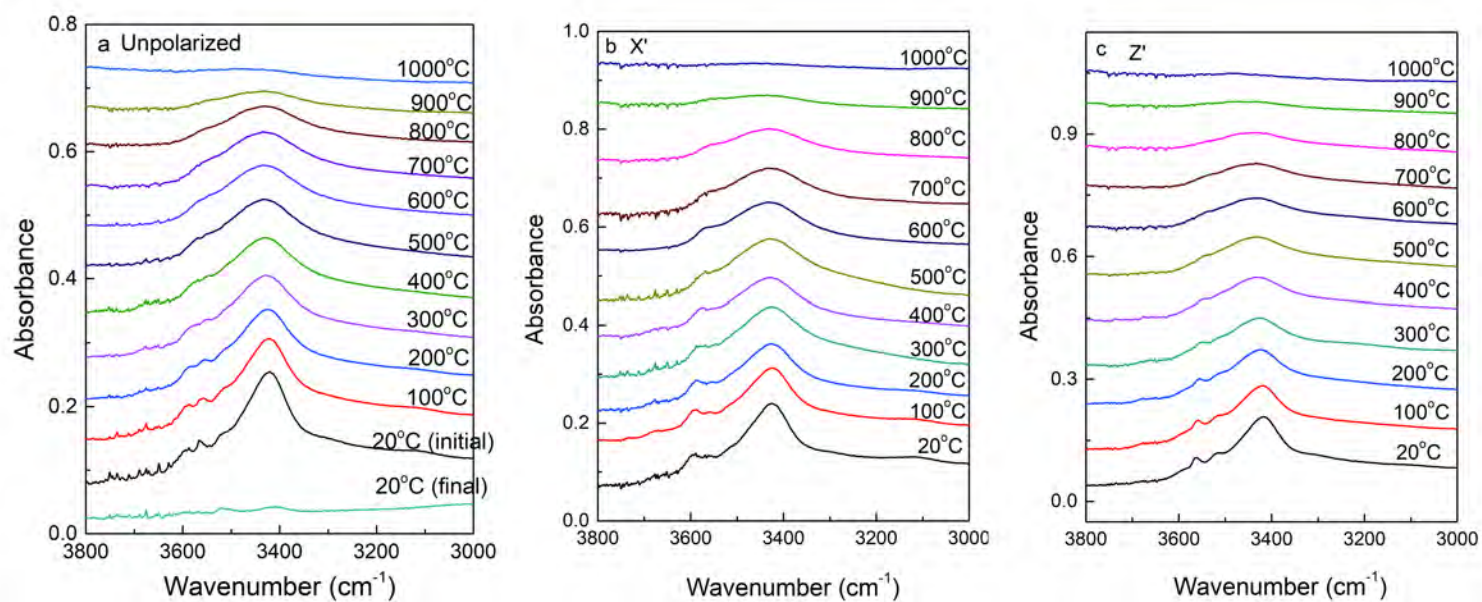
703

704

705

706

707
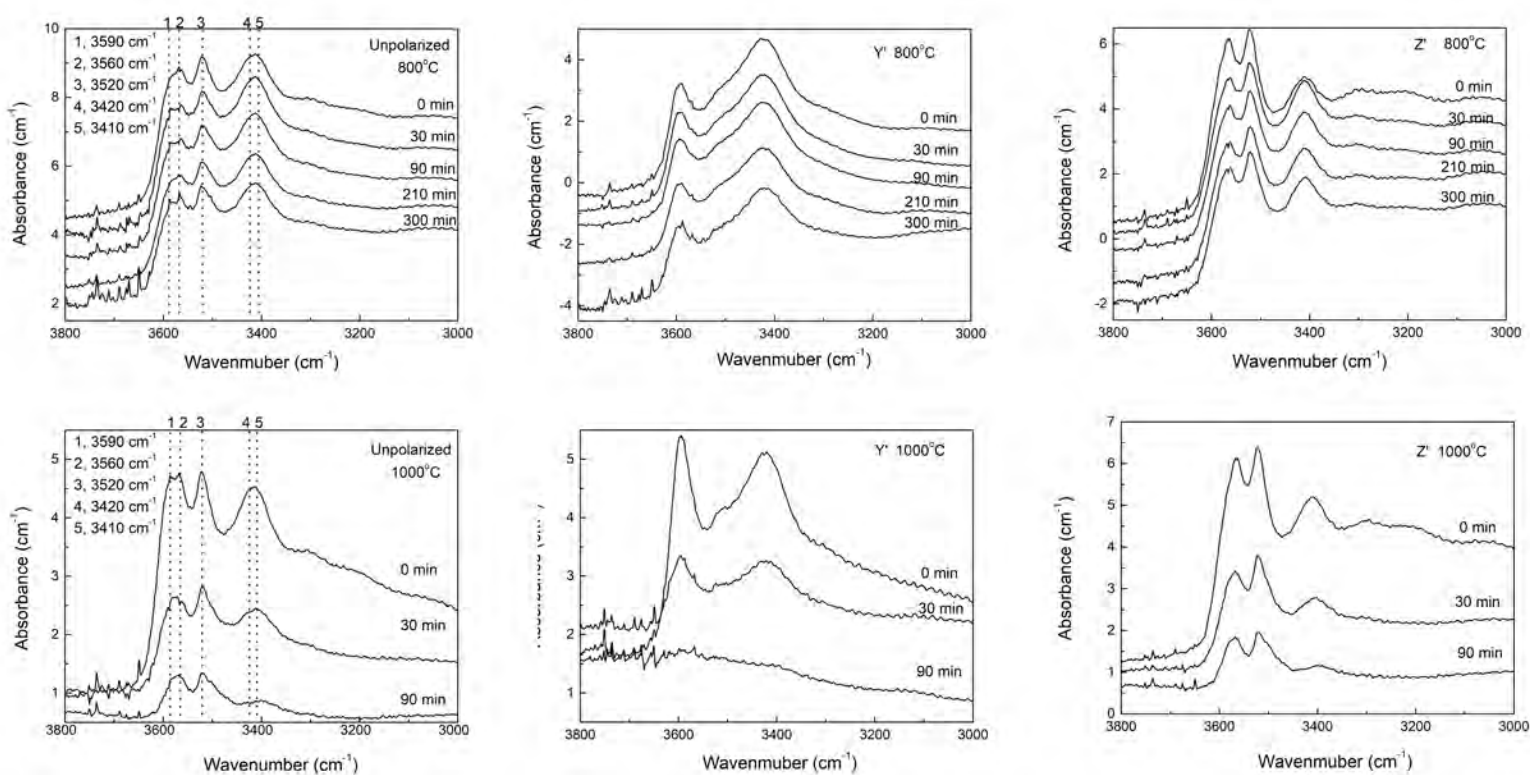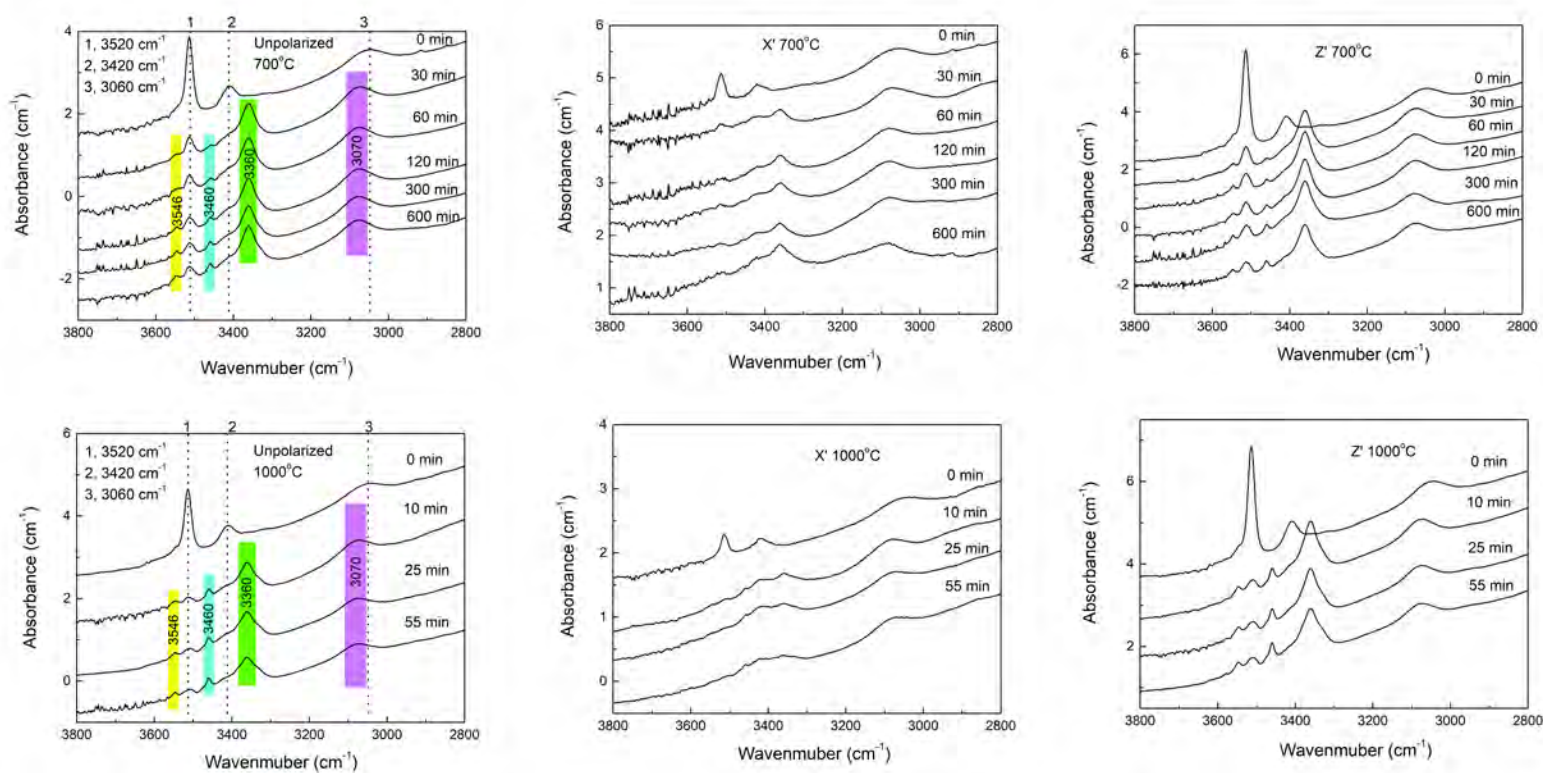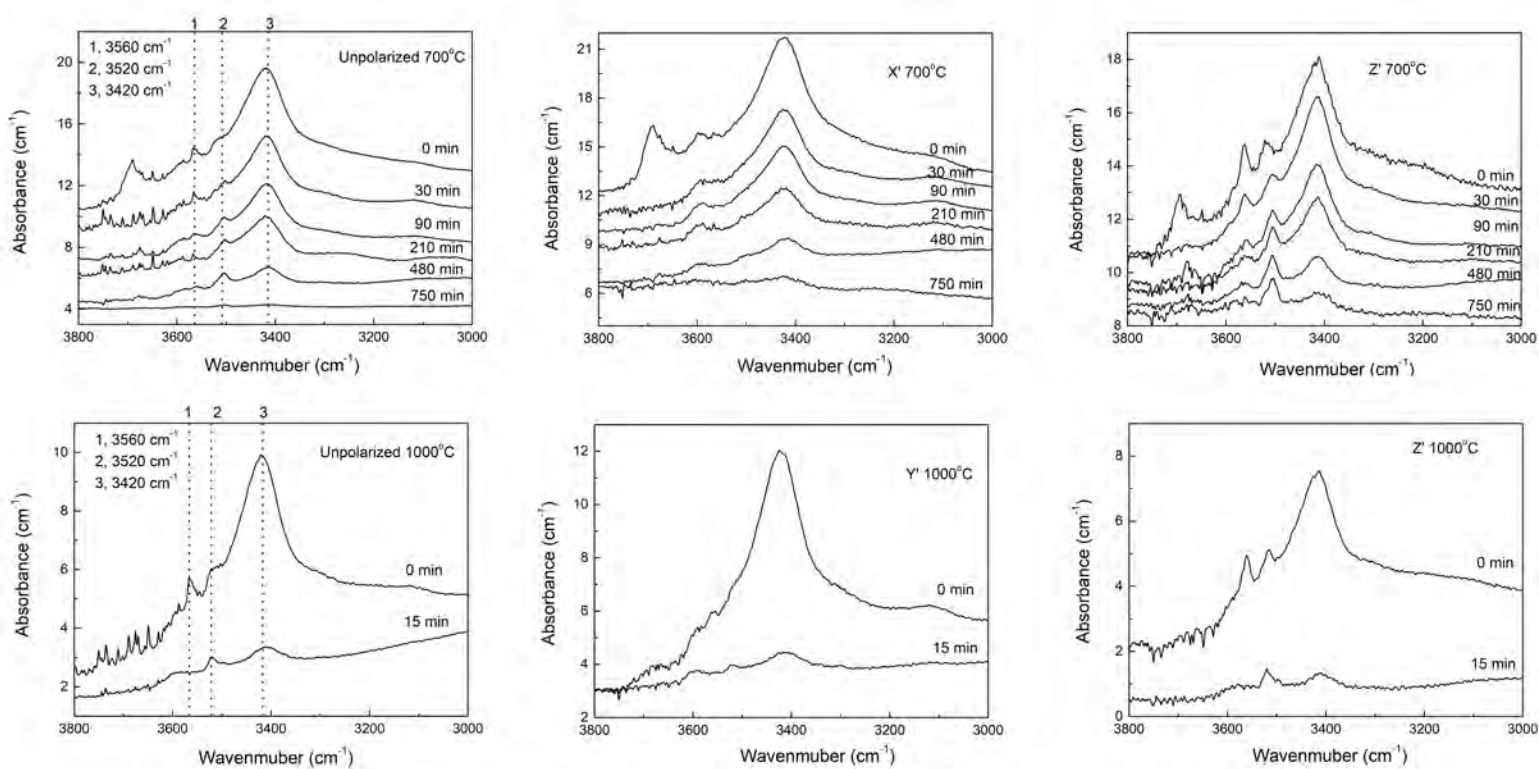
708

709
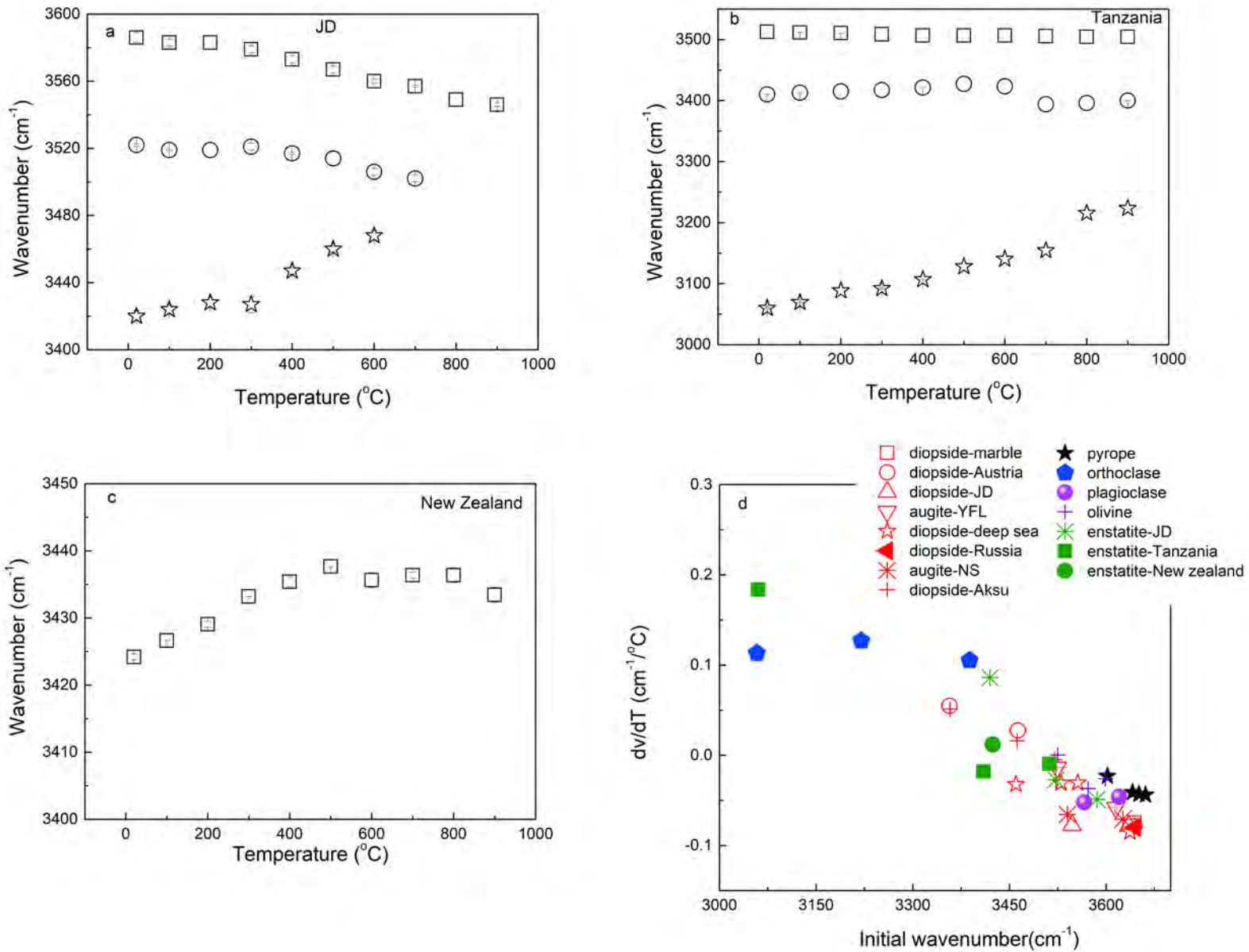
710

711

712

Figure 1

Figure 2

Figure 3

Figure 4

Figure 5

Figure 6

Figure 7

Figure 8

Figure 9